Spectral pixels as images: CNN-based pixel classification of 4D hyperspectral data for nerve and ligament differentiation

Naira Matosyan[a,b], Narek Chilingaryan[c], Narine Sarvazyan[a,c,d], and Varduhi Yeghiazaryan[a]

[a]American University of Armenia, Yerevan, Armenia
[b]Yerevan State University, Yerevan, Armenia
[c]L. A. Orbeli Institute of Physiology NAS RA, Yerevan, Armenia
[d]George Washington University, Washington, DC, United States

ABSTRACT

Hyperspectral imaging is actively gaining popularity for multiple biomedical applications due to its ability to capture rich information from the electromagnetic spectrum. In particular, it can be used to differentiate multiple tissues based on their fluorescence. The reliable differentiation of nerve and ligament tissues is of particular interest in the surgical setting since these tissues have similar appearance for the human vision. By exciting the tissue with several consecutive wavelength bands from the longwave ultraviolet range and registering the tissue response in the visible light range, we construct a 4D hyperspectral image. We present a very first investigation into tissue classification from 4D hyperspectral images through a novel approach that treats excitation–emission matrices of individual pixels as images and trains a deep convolutional neural network for their classification. We test our approach on four different datasets of nerve and ligament tissue excised from bovine trotters, with variable imaging conditions. We achieve an impressive 94–99% classification accuracy with only 1% of pixels used as training data. We further examine cross-dataset applicability of the trained deep neural models and their sensitivity to changes in imaging conditions. Finally, our approach is benchmarked against and is shown to be superior by 10.4%, on average, to established automated analysis techniques like linear unmixing for biomedical hyperspectral images.

Keywords: 4D hyperspectral imaging, CNN, pixel classification, nerve detection

1. INTRODUCTION

Hyperspectral imaging (HSI) is a promising tool for contact-free detection/visualization of surgical targets, such as nerves or other tissues. HSI is a rapidly growing field that has not yet reached research saturation according to bibliometric indicators.[1] It has been applied to a wide range of problems from estimating ink age[2] and chronological order of crossing lines[3] on documents for forensic purposes, to counterfeit drug detection[4] and image-guided surgery[5] in healthcare and medical fields. Various approaches have been developed for different stages of the imaging-to-analysis process to enhance the characterization and differentiation of objects of interest. One of the emerging developments is the enhancement of the usual 3D hyperspectral data with a 4^{th} dimension, be that temporal,[6] spatial,[7] or spectral.[8,9] Spectral enhancement of data, also called multi-excitation hyperspectral autofluorescence imaging,[10] is the compilation of one 4D dataset out of multiple 3D hyperspectral fluorescence images of the same sample acquired under different excitation conditions. The rationale behind spectral enhancement of HSI is that certain fluorophores may not be detectable or differentiable under a single excitation condition, but may require multiple illumination settings.

Inadvertent nerve damage occured during clinical procedures, also called iatrogenic nerve injury (INI), is a significant challenge in the surgical field, causing non-negligible rates of postoperative morbidity in patients. As Throckmorton et al.[11] report, INIs occur in 40–60% of complex surgeries such as mastectomies and prostatectomies, and comprise 400,000 to 600,000 cases annually in the US. Such an incidence can be partly attributed to visual similarity of nerves with other tissues, like ligaments and tendons.

Further author information: (Send correspondence to N.M.)
N.M.: naira_matosyan19@alumni.aua.am N.Ch.: narek.chilingaryan@physiol.sci.am
N.S.: nsarvazyan@aua.am V.Y.: vyeghiazaryan@aua.am

Medical Imaging 2025: Image Processing, edited by Olivier Colliot, Jhimli Mitra, Proc. of SPIE Vol. 13406, 1340629 · © 2025 SPIE
1605-7422 · doi: 10.1117/12.3047194

Several studies[11–17] have explored various diffuse reflectance HSI and spectroscopic techniques for nerve identification. Others[18–20] have used cumulative autofluorescence to visualize nerve tissue. However, to the best of our knowledge, autofluorescence-based HSI in general, and 4D HSI in particular, have never been utilized for nerve differentiation.

Image analysis of HSI data includes data preprocessing, feature extraction and selection, and spectral unmixing or pixel classification. Among supervised classification algorithms support vector machines, artificial neural networks, spectral information divergence, and spectral angle mappers have been commonly used.[21] Recently convolutional neural networks (CNN) have gained popularity in HSI applications. Based on the input HSI data dimensionality, CNN models have been categorized into: spectral (applying 1D convolutions on individual spectral profiles), spatial (applying 2D convolutions on pixel neighborhoods, treating spectral bands as channels) and spectral–spatial (applying 3D convolutions on pixel neighborhoods and all spectral bands) models.[22] However, given the novelty of 4D autofluorescence HSI, CNNs have not yet been applied to biomedical 4D HSI data.

We propose a novel approach of CNN-based pixel classification of 4D HSI data for the automated differentiation of nerve and ligament tissues. A 4D HSI dataset can be interpreted as a rectangular arrangement of (x, y) pixels, where every pixel contains data across two spectral axes, forming an excitation–emission matrix (EEM). We treat the EEM of each pixel as a small image and train a CNN to classify these per tissue type. While extensive studies exist on the automated classification of pixels in traditional 3D HSI, using machine learning, in general, and deep learning, in particular, to the best of our knowledge, this is a first attempt at 4D HSI classification using deep CNN.

2. MATERIALS AND METHODS

We consider 4D hyperspectral datasets, illustrated in Fig. 1, acquired from four bovine nerve and ligament sample preps using different preparation and imaging conditions.

2.1 Specimens and Sample Preparation

Bovine trotters, some fresh and some frozen, were acquired from local butchers. Nerve and ligament tissues were isolated, transferred to plastic Petri dishes. Tissues were attached using a tape to the bottom of Petri dishes in order to avoid any movement during image acquisition, as well as covered with 0.9% NaCl (normal saline) to prevent drying.

2.2 Imaging Setup and Auxiliary Measurements

For illuminating the samples at different wavelengths, TLS130B-300X tunable light source was used, with 77330 focusing lens assembly mounted in order to maximize the light output. Light delivery to samples was carried out using a concave simple mirror in case of samples 240618 and 240701, and a flat TECHSPEC 50 mm enhanced deep ultraviolet (DUV) mirror in case of samples 240718 and 240730. Light output (optical power) at approximately sample position was measured using Newport Power Meter 1936-R and 918D-UV-OD3R photodiode sensor, in order to account for light intensity wavelength-dependent changes across different illumination conditions. Nuance FX imaging system was used for hyperspectral data acquisition.

2.3 4D Hyperspectral Image Acquisition

4D datasets (available at https://zenodo.org/communities/nar-sar-iph/) were obtained by acquiring 3D hyperspectral images at different excitation (illumination) conditions, described by the fourth—excitation wavelength (λ_{ex})—dimension, in addition to the classical two spatial (x, y) and one spectral (λ_{em}) dimensions of 3D datasets. Specifically, samples were subsequently illuminated by near-monochromatic light ranging from 300 to 400 nm of wavelength at 10 nm intervals. Under each illumination condition 3D hyperspectral images (hereafter interchangeably referred to as cubes) were acquired using Nuance FX imaging system, collecting autofluorescence signal from 420 to 720 nm at 10 nm intervals, exposure time set to maximum—5000 ms. Thus, each pixel EEM has 11 values along the λ_{ex} axis and 31 values along the λ_{em} axis. Background (with no illumination) and white-light illumination images were also obtained for data correction and RGB visualization purposes for each dataset. The sizes and spatial resolutions of the datasets are different: sample 240618 is 520×400 pixels, sample 240701 is 406×464, 240718 is 1300×1040, and sample 240730 is 1136×1032.

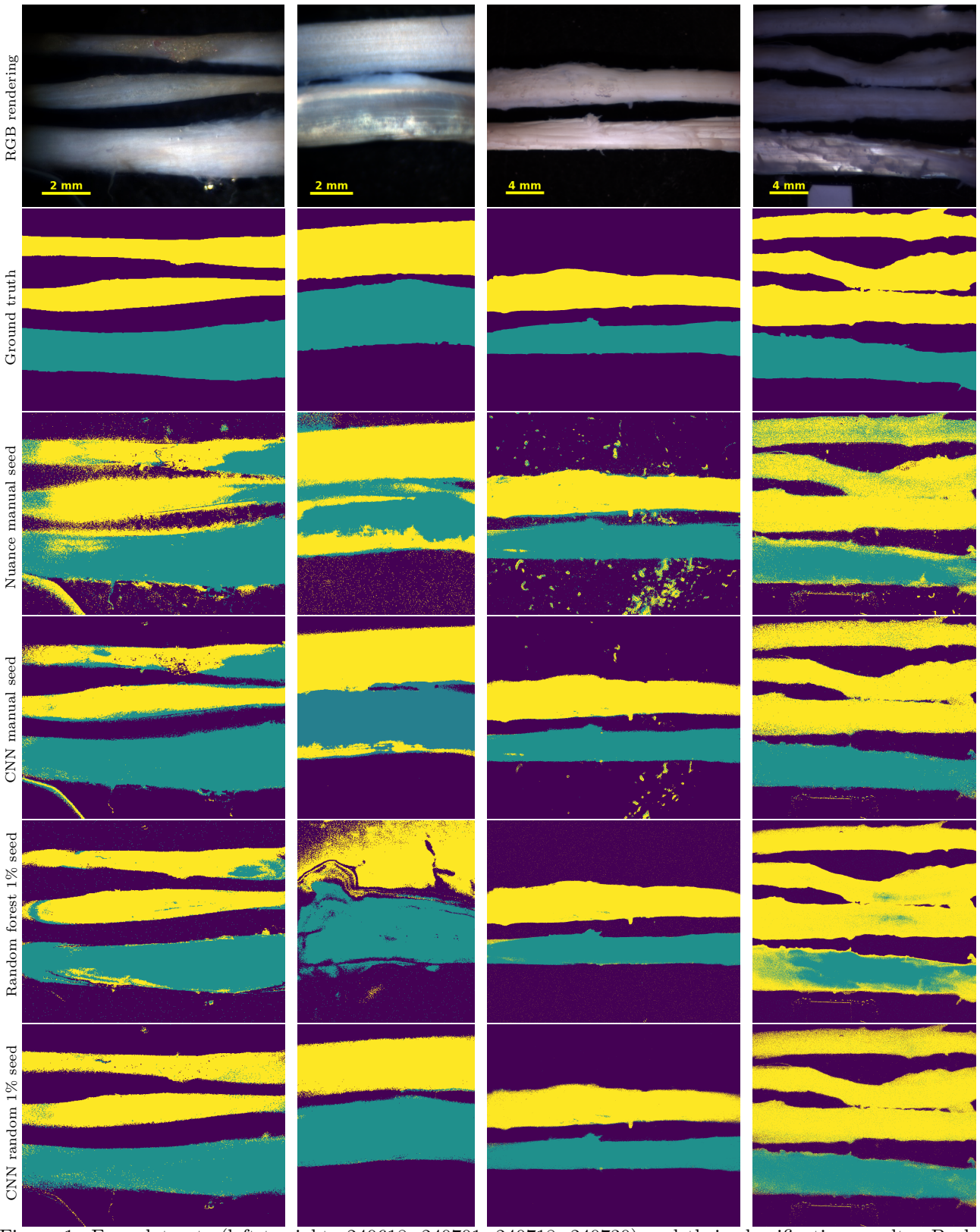

Figure 1: Four datasets (left-to-right: 240618, 240701, 240718, 240730) and their classification results. Background shade is purple, nerve is in yellow, ligament is in teal.

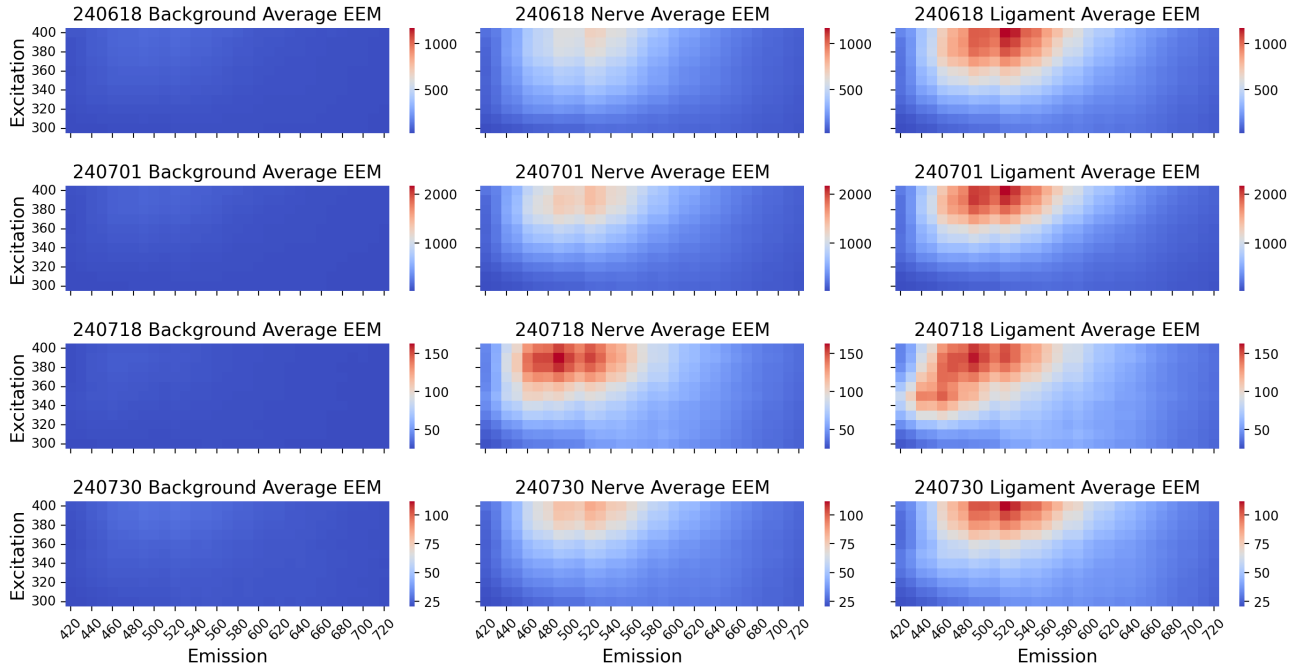

Figure 2: Average EEMs from raw data per semantic class—background, nerve, and ligament—for all four datasets. Excitation and emission wavelengths are in nanometers.

For each dataset, a three-class mask was manually generated to differentiate the nerve tissue (in yellow), ligament (in teal), and background (in purple). These masks can be seen in the second row of Fig. 1. Figure 2 shows average EEMs, constructed based on these ground-truth masks, to illustrate the spectral features of each class. Ligament EEMs show a stronger autofluorescence pattern than nerve EEMs. Sample 240718 deviates from this pattern, with extra fluorescence observed in lower emission and/or excitation wavelengths. This can be explained by the biological material preservation conditions; this sample had been kept in a freezer before acquisition. Background EEMs are also provided for reference. The variability of raw and preprocessed data for nerve and ligament tissues is shown in Fig. 3, expressed in means and standard deviations.

2.4 CNN Architecture

The data was subjected to several steps of correction to eliminate signal resulting from ambient stray light reflectance and the effect of illumination light intensity. Then, the resulting EEMs for each pixel were considered as separate images with a size of 11×31, normalized based on the maximum of each EEM.

The proposed CNN architecture consists of three convolutional layers with ReLU activations, each followed by max pooling to progressively reduce the spatial dimensions, while increasing feature depth. The first convolutional layer uses 32 filters, expanding to 64 filters in subsequent layers, all with a kernel size of 3×3 and padding of 1. After the convolution and pooling layers, the feature map is flattened and processed through two fully connected layers, ending with an output layer designed for a three-class classification. The model was trained over 200 epochs using a cross-entropy loss function. The Adam optimizer was used with a learning rate of 0.001 to update the model's parameters efficiently.

3. RESULTS

3.1 Train–Test Splits

To estimate the performance of the CNN for each dataset, six different train–test split sizes of all pixels were considered. With a factor of 5, the training set size ranged from 0.008% of pixels to 25%. Per size, five different random train–test splits were executed. Average test accuracies are reported in Fig. 4. The boxplots show

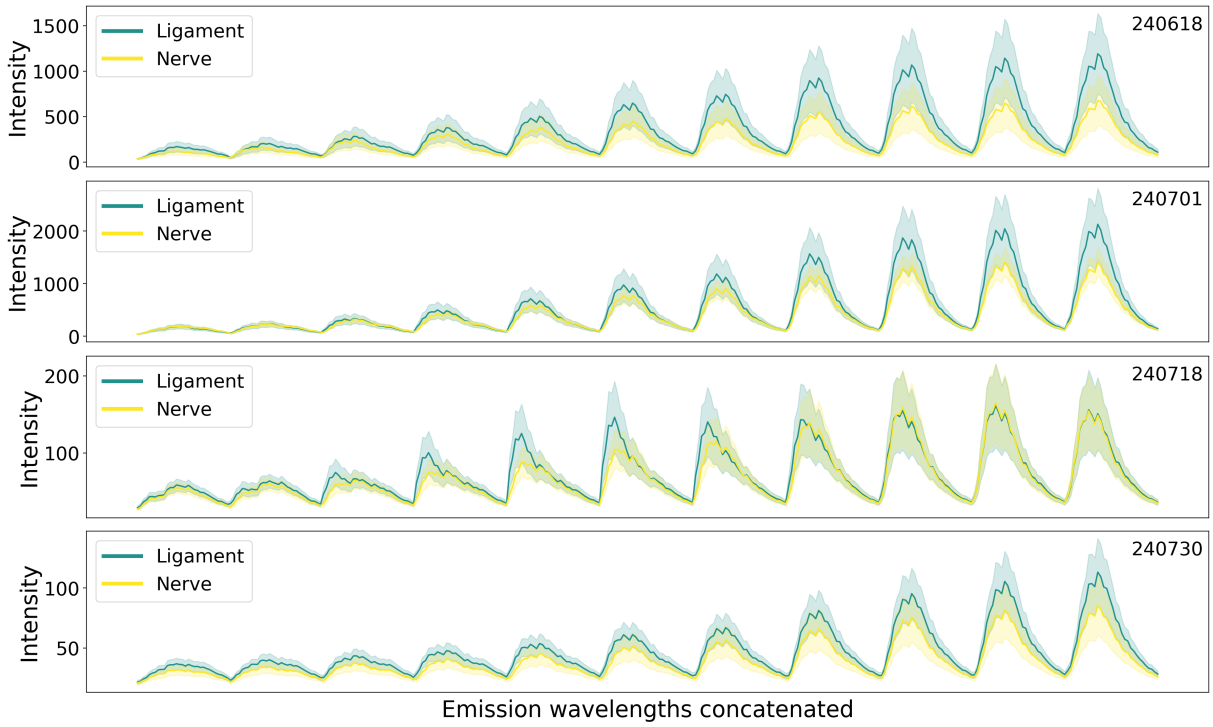

(a) Raw

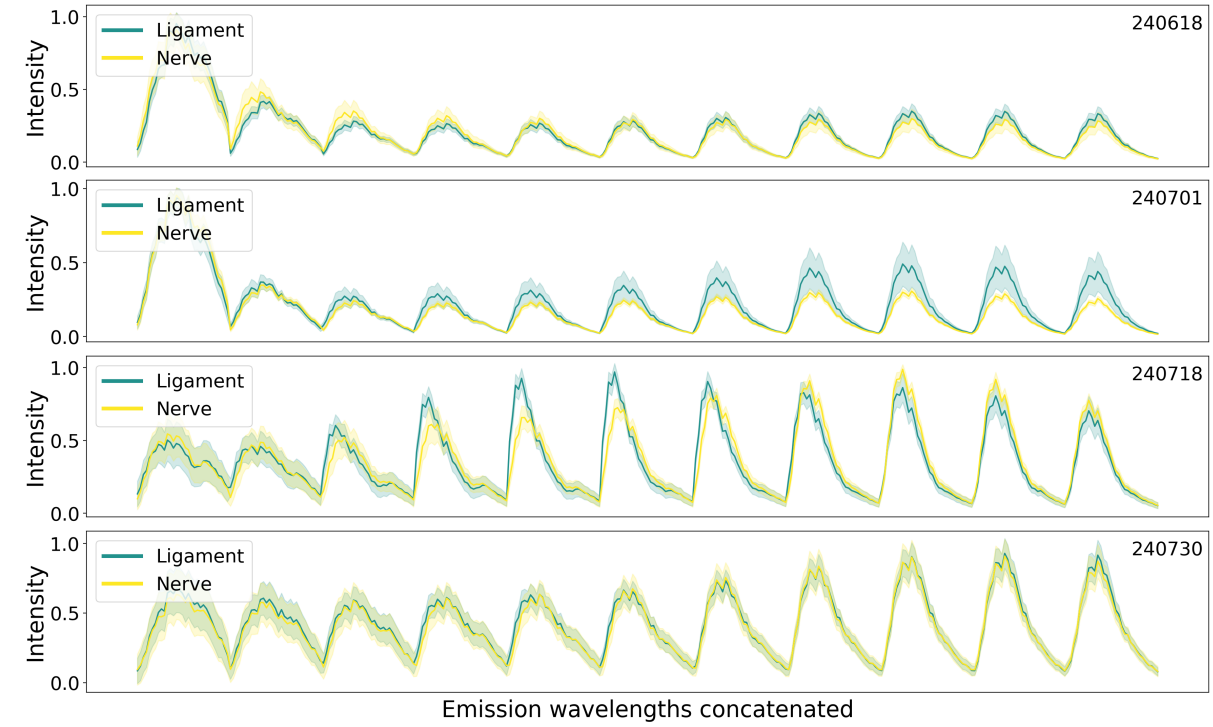

(b) Preprocessed

Figure 3: Lineplots showing the average and standard deviation of emission intensity from nerve and ligament tissues in (a) raw and (b) preprocessed data (1000 pixels per class), by dataset and emission wavelength. Preprocessing includes background subtraction, correction by light source intensity, and, for each pixel, normalization of concatenated spectrum by its maximum.

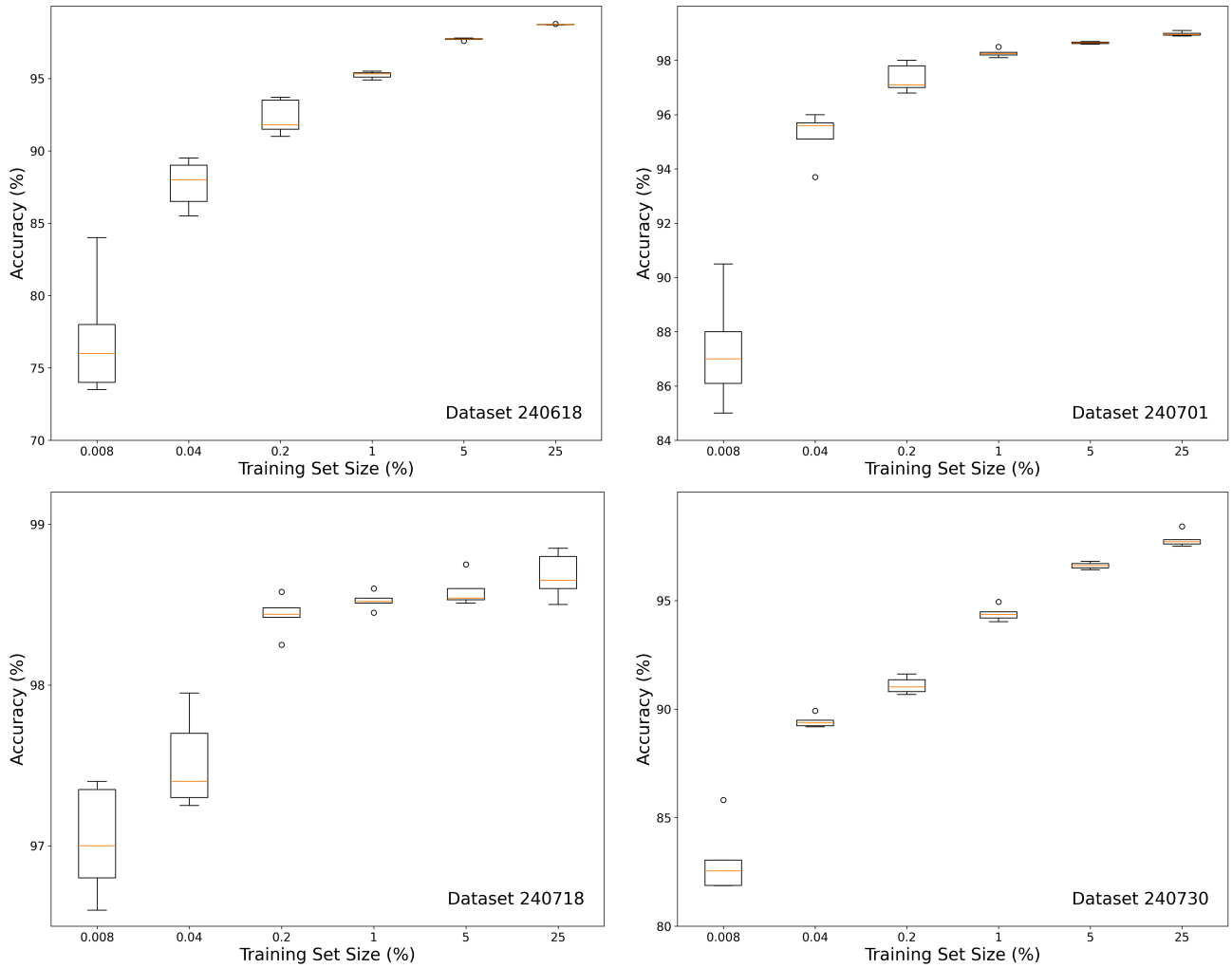

Figure 4: Classification accuracy boxplots for 6 different training set sizes (0.008%, 0.04%, 0.2%, 1%, 5%, 25%). For each training setup, five different random train–test splits are utilized.

that the accuracy starts stabilizing from the 1% training set. Thus, a 1% train and 99% test split is utilized in further experiments to achieve high performance while keeping the training set small. The model reaches 94–99% impressive accuracy on the test set (99% of all pixels) across the four 4D HSI datasets. Additionally, on sample 240718 the CNN achieves classification accuracy of around 97% even for the smallest training set of 0.008% of pixels. This can be attributed to the larger spatial size of this dataset in comparison with the other two, leading to an increased absolute number of training samples even in the 0.008% split. The bottom row of Fig. 1 shows the resulting predicted labels to be comparable to the ground truth masks in the second row.

3.2 Comparison with Traditional Machine Learning Approaches

To evaluate the effectiveness of our proposed method, we compared its performance with several well-established machine learning (ML) techniques—including logistic regression, support vector machine, K-nearest neighbors, decision tree, random forest and naive Bayes—using the same 1% of the data for training. Table 1 summarizes resulting classification accuracies for all algorithms. While some classical models, such as random forest, displayed relatively strong accuracies (up to 93.72% on the 240618 dataset), the CNN consistently outperformed all other methods across all four datasets, achieving accuracies of up to 98.36%. This robust performance with minimal training data underscores the superior capacity of the CNN to capture the underlying excitation–emission patterns in 4D HSI, making it a highly suitable choice for tissue classification.

Table 1: Comparison between different ML models based on 1% training size. The best accuracies are in bold, the second best are underlined, and third results are italicized.

Model \Dataset	**240618**	**240701**	**240718**	**240730**
Logistic regression	*92.24%*	70.10%	97.74%	*91.83%*
Support vector machine	88.36%	70.27%	<u>98.33%</u>	<u>92.72%</u>
K-nearest neighbors	91.71%	73.89%	98.12%	85.30%
Decision tree	89.63%	*73.90%*	96.73%	82.31%
Random forest	<u>93.72%</u>	<u>82.24%</u>	*98.22%*	87.18%
Naive Bayes	81.23%	55.92%	90.80%	71.82%
CNN	**95.33%**	**98.27%**	**98.36%**	**94.36%**

3.3 Cross-Dataset Testing

As the EEMs were normalized before feeding into the CNN, cross-dataset classification was attempted by applying the 1%-training-data models from Sec. 3.1 on all pixels from other datasets. Table 2 summarizes resulting classification accuracies. Due to the significant differences in the sample preparation and imaging conditions of the datasets, low scores are expected. However, the model trained on pixels from sample 240701 gets around 74% and 79% accuracies on samples 240618 and 240718, respectively. Furthermore, leave-one-group-out cross-validation was performed, where models were trained on 100% of the data from three datasets and tested on 100% of the remaining one (Table 3). This approach did not yield further improvements over the cross-dataset classification accuracies in Table 2. Additional experiments on multiple datasets with standardized imaging conditions are required to estimate the real potential of the method for cross-dataset testing.

Table 2: Cross-dataset accuracy matrix based on 1% training size models.

Train 1% \Test	**240618**	**240701**	**240718**	**240730**
240618	95.33%	62.95%	67.33%	50.03%
240701	73.81%	98.27%	79.26%	55.94%
240718	53.69%	52.65%	98.36%	70.29%
240730	62.93%	67.00%	68.47%	94.36%

Table 3: CNN accuracies based on leave-one-group-out cross validation.

Train \Test	**240618**	**240701**	**240718**	**240730**
All Except Test	70.70%	49.17%	84.12%	51.96%

3.4 Comparison with Other HSI Analysis Approaches

We used Nuance 3.0.2 software to perform standard linear unmixing based on manual region of interest (ROI) selection. In order to unmix the 4D HSI, the cubes of 300–400 nm excitation wavelengths were sequentially combined along their emission axis. More details can be found in the companion paper.[9] ROIs were selected so as to comprise maximally representable samples of pixels from each class, with a total number close to the 1% target. Unmixing results were converted into classification masks (Fig. 1, row 3) and compared with the CNN predictions (Fig. 1, row 4), using the same ROIs as training sets. The CNN demonstrated notable accuracy improvements: from 75.93% to 89.81% for sample 240618 and from 79.40% to 91.98% for sample 240701. Similarly, accuracy increased from 89.29% (unmixing) to 96.71% (CNN) for sample 240718 and from 84.71% to 92.30% for sample 240730. The average accuracy improvement was 10.37%.

4. CONCLUSION

This paper presents a novel approach for the analysis of spectrally enhanced HSI, by interpreting the EEMs of individual pixels as images and using a simple deep CNN for their classification. Our CNN-based approach shows very high classification accuracies in the intra-dataset setting. While cross-dataset predictions are promising, they suggest that standardization of the data acquisition process and/or additional processing steps are needed for good performance. Benchmarking against traditional ML approaches (with random training sets) and linear unmixing (with ROI-based training sets) clearly shows the superiority of our method for *ex vivo* nerve and ligament differentiation in 4D HSI. Our experimental results indicate that there is potential to further explore the applicability of the proposed approach for high-accuracy classification of tissues in a cross-dataset setting, especially for intraoperative datasets for various surgical targets. In future work, we plan to explore *in vivo* nerve and ligament differentiation from 4D HSI and to utilize more complex deep learning architectures.

ACKNOWLEDGMENTS

We are grateful to Ani Avetisyan for consultations regarding Nuance FX software and to Fernando Villarruel and Tigran Soghomonyan for help in data acquisition. Financial support of the European Union (NAR-SAR-IPH-101087403) and Afeyan Family Foundation AUA Research Grant Program is gratefully acknowledged. This research has benefited from the Professional Development Program of the American University of Armenia in 2025, the Short Term Conference and Travel Grant of the Calouste Gulbenkian Foundation, the Armenian Fellowships Program of the H. Hovnanian Family Foundation, and the SPIE Student Conference Support program.

REFERENCES

[1] Jiang, S., Ma, D., Tan, X., Yang, M., Jiao, Q., and Xu, L., "Bibliometric analysis of the current status and trends on medical hyperspectral imaging," *Frontiers in Medicine* **10**, 1235955 (2023).

[2] Zaman, Z., Ahmed, S. B., and Malik, M. I., "Analysis of hyperspectral data to develop an approach for document images," *Sensors* **23**(15), 6845 (2023).

[3] Martins, A. R., Dourado, C. S., Talhavini, M., Braz, A., and Braga, J. W. B., "Determination of chronological order of crossed lines of ballpoint pens by hyperspectral image in the visible region and multivariate analysis," *Forensic Science International* **296**, 91–100 (2019).

[4] Wilczyński, S., Koprowski, R., Marmion, M., Duda, P., and Błońska-Fajfrowska, B., "The use of hyperspectral imaging in the vnir (400–1000 nm) and swir range (1000–2500 nm) for detecting counterfeit drugs with identical api composition," *Talanta* **160**, 1–8 (2016).

[5] Barberio, M., Benedicenti, S., Pizzicannella, M., Felli, E., Collins, T., Jansen-Winkeln, B., Marescaux, J., Viola, M. G., and Diana, M., "Intraoperative guidance using hyperspectral imaging: a review for surgeons," *Diagnostics* **11**(11), 2066 (2021).

[6] Noda, I., "Two-dimensional correlation spectroscopy (2D-COS) analysis of evolving hyperspectral images," *Applied Spectroscopy* **79**(1), 77–86 (2025).

[7] Li, J., Zheng, Y., Liu, L., and Li, B., "4D line-scan hyperspectral imaging," *Optics Express* **29**(21), 34835–34849 (2021).

[8] Chaumel, J., Marsal, M., Gómez-Sánchez, A., Blumer, M., Gualda, E. J., de Juan, A., Loza-Alvarez, P., and Dean, M. N., "Autofluorescence of stingray skeletal cartilage: hyperspectral imaging as a tool for histological characterization," *Discover Materials* **1**(1), 16 (2021).

[9] Chilingaryan, N., Villarruel, F., Soghomonyan, T., Yeghiazaryan, V., and Sarvazyan, N., "4D hyperspectral imaging for intraoperative tissue classification," in [*Medical Imaging 2025: Clinical and Biomedical Imaging*], SPIE (2025).

[10] Ghaffari, M., Chateigner-Boutin, A.-L., Guillon, F., Devaux, M.-F., Abdollahi, H., and Duponchel, L., "Multi-excitation hyperspectral autofluorescence imaging for the exploration of biological samples," *Analytica Chimica Acta* **1062**, 47–59 (2019).

[11] Throckmorton, G. A., Haugen, E., Thomas, G., Willmon, P., Baba, J. S., Solórzano, C. C., and Mahadevan-Jansen, A., "Label-free intraoperative nerve detection and visualization using ratiometric diffuse reflectance spectroscopy," *Scientific Reports* **13**(1), 7599 (2023).

[12] Schols, R. M., Ter Laan, M., Stassen, L. P., Bouvy, N. D., Amelink, A., Wieringa, F. P., and Alic, L., "Differentiation between nerve and adipose tissue using wide-band (350–1,830 nm) in vivo diffuse reflectance spectroscopy," *Lasers in Surgery and Medicine* **46**(7), 538–545 (2014).

[13] Nouri, D., Lucas, Y., and Treuillet, S., "Hyperspectral interventional imaging for enhanced tissue visualization and discrimination combining band selection methods," *International Journal of Computer Assisted Radiology and Surgery* **11**, 2185–2197 (2016).

[14] Maktabi, M., Köhler, H., Ivanova, M., Neumuth, T., Rayes, N., Seidemann, L., Sucher, R., Jansen-Winkeln, B., Gockel, I., Barberio, M., et al., "Classification of hyperspectral endocrine tissue images using support vector machines," *The International Journal of Medical Robotics and Computer Assisted Surgery* **16**(5), 1–10 (2020).

[15] Barberio, M., Collins, T., Bencteux, V., Nkusi, R., Felli, E., Viola, M. G., Marescaux, J., Hostettler, A., and Diana, M., "Deep learning analysis of in vivo hyperspectral images for automated intraoperative nerve detection," *Diagnostics* **11**(8), 1508 (2021).

[16] Haugen, E. J., Throckmorton, G. A., Walter, A. B., Mahadevan-Jansen, A., and Baba, J. S., "Measurement of rat and human tissue optical properties for improving the optical detection and visualization of peripheral nerves," *Biomedical Optics Express* **14**(6), 2839–2856 (2023).

[17] Tran, M. H., Bryarly, M., Ma, L., Yousuf, M. S., Price, T. J., and Fei, B., "Nerve detection and visualization using hyperspectral imaging for surgical guidance," in [*Medical Imaging 2024: Clinical and Biomedical Imaging*], Gimi, B. S. and Krol, A., eds., **12930**, 129302A, SPIE (2024).

[18] Dip, F., Aleman, R., Socolovsky, M., Villalba, N., Falco, J., Menzo, E. L., White, K. P., and Rosenthal, R. J., "Nerve spectroscopy: understanding peripheral nerve autofluorescence through photodynamics," *Surgical Endoscopy* , 1–8 (2021).

[19] Dip, F., Rosenthal, D., Socolovsky, M., Falco, J., De la Fuente, M., White, K. P., and Rosenthal, R. J., "Nerve autofluorescence under near-ultraviolet light: cutting-edge technology for intra-operative neural tissue visualization in 17 patients," *Surgical Endoscopy* , 1–11 (2022).

[20] Dip, F., Bregoli, P., Falco, J., White, K. P., and Rosenthal, R. J., "Nerve autofluorescence in near-ultraviolet light markedly enhances nerve visualization in vivo," *Surgical Endoscopy* , 1–7 (2022).

[21] Lu, G. and Fei, B., "Medical hyperspectral imaging: a review," *Journal of Biomedical Optics* **19**(1), 010901–010901 (2014).

[22] Yoon, J., "Hyperspectral imaging for clinical applications," *BioChip Journal* **16**(1), 1–12 (2022).